RESEARCH ARTICLE

A new open-source solver for early detection of atherosclerosis based on hemodynamics and LDL transport simulation

Jorge Molina[1] | Daniel Rhys Obaid[2] | A. S. Ademiloye[3,4]

[1]Esc. Ing. Caminos, Campus Fuentenueva, University of Granada, Granada, Spain

[2]Swansea University Medical School, Singleton Campus, Swansea, UK

[3]Zienkiewicz Institute for Modelling, Data and AI, Faculty of Science and Engineering, Swansea University, Bay Campus, Swansea, UK

[4]Department of Biomedical Engineering, Faculty of Science and Engineering, Swansea University, Bay Campus, Swansea, UK

Correspondence
Jorge Molina, Esc. Ing. Caminos, Campus Fuentenueva, University of Granada, 18071, Granada, Spain.
Email: jorgemolina@ugr.es

Abstract

This article presents a new open-source solver within the OpenFOAM framework, to provide a cost-free alternative to commercial software for simulating blood flows and the transport of low-density lipoproteins (LDL) in arteries. The proposed algorithm utilizes the velocity field obtained from the hemodynamics computation to solve an advection-diffusion equation governing a passive scalar variable, that represents the cholesterol concentration in blood. Moreover, two customized boundary conditions, namely periodic pulsatile inflow and LDL blood-to-wall transfer law, as well as a non-Newtonian viscosity model, are included in the code to achieve more realistic results. The solver is first validated by reproducing two benchmark tests, the classical lid-driven cavity experiment including heat transport, and a constricted tube simulating a stenosed artery. The results obtained were in good agreement with existing literature and experimental measurements, thus confirming the accuracy and robustness of the proposed open-source solver. Finally, hemodynamics and LDL transport are computed in two arteries, one of them obtained by segmentation from an anonymized clinical patient. Stress and LDL concentration at the vessel's wall are employed to calculate significant descriptors revealing dangerous areas where atherosclerotic plaques could emerge. In the studied cases, the main branch of the artery, and especially the vicinity of the bifurcation, seem to be candidates to develop the illness. This conclusion is in line with medical in-vivo studies evincing that bifurcations are an usual place where plaques grow.

KEYWORDS

atherosclerosis, hemodynamics, LDL transport, numerical modeling, OpenFOAM, open-source

1 | INTRODUCTION

Cardiovascular diseases (CVDs) are the primary global cause of mortality, taking an estimated 17.9 million lives every year, according to the World Health Organization.[1] Among CVDs, coronary artery atherosclerosis is the leading cause of death for both women and men in developed countries.[2] This common disease occurs when fatty deposits, known as

atheromatous plaques, accumulate in the inner layers of arteries. These deposits grow due to the proliferation of fibrous tissues and surrounding smooth muscle. The resulting inflammatory lesion causes a reduction in blood flow and, in the worst case, rupture of the artery, leading to the formation of a thrombus and the subsequent heart attack or ischemic stroke (85% of deaths from CVDs were caused by these events).[1,3]

The proliferation of atheromatous plaques begins with the permeation and accumulation of high molecular weight solutes delivered from streaming blood in the arterial intima, particularly high levels of low-density lipoproteins (LDL) (see e.g., References [4] and [5]). The resulting inflammatory lesion progressively grows during several years, even decades, changing the structure of the host's artery.[6] In addition to the narrowing and restriction of blood flow, arteries harden,[7] and changes in the integrity of the arterial plaque can make them more susceptible to potential ruptures.

Traditional risk factors for cardiovascular diseases, such as aging, high levels of LDL, high blood pressure, or smoking, cannot fully account for the risk of the atherosclerosis progression (see Reference [8] and references therein). Among the known risk factors, high levels of LDL have a clear relationship with the pathological process of atherosclerotic plaque development.[9] This is because LDL particles, along with blood platelets, penetrate the thin layer of endothelial cells when it is damaged. Then, in the layer below, smooth-muscle cells and macrophages ingest and degrade LDL and become foam cells. Thus, if the blood LDL level is too elevated, cholesterol derived from the LDL accumulates in and among the foam cells, constituting an atheroma (see e.g., References [10] and [11]).

Conversely, hemodynamics has also been demonstrated to be essential in the prediction of the proliferation, growth, and rupture of atheromatous plaques. In this aspect, computational fluid dynamics (CFD) is one of the most valuable non-invasive tools to know important hemodynamic measures such as the wall shear stress (WSS), that has been used as indicator in several investigations (see e.g., References [5,12–14]). Furthermore, CFD can be combined with computed tomography, angiography or other medical imaging to attain patient-specific inputs for the numerical model, and thus achieve more accurate, realistic, and reliable hemodynamic outcomes.[4,5,15,16] In addition, these results can also be used as inputs for artificial intelligence based models, which have gained importance in recent years (see e.g., References [17] and [18]). The numerical quantification of LDL concentration and WSS on the arterial intima requires a complex three-dimensional model to solve the hemodynamics and a coupled advection-diffusion equation considering, among others, the pulsatile flow and the non-Newtonian behavior of blood.[19] For this reason, researchers normally resort to expensive commercial software to perform their investigations (see e.g., References [19–25]) instead of using free and open-source alternatives, usually less user-friendly. Hence, it seems evident that there is a need for wider availability of free software to facilitate the access to advanced tools for hemodynamics simulations in arteries.

This work introduces a new freely available solver within the OpenFOAM framework[26] to compute hemodynamics and LDL transport in patient-specific arteries, thus providing an open-source alternative to commercial software for investigators and experts focused on cardiovascular disease research. OpenFOAM is a well-known library with several advantages, such as code customization, parallelization, meshing tools, and linkability to external codes. It is based on the Finite Volume Method and incorporates numerous solvers for the simulation of incompressible and compressible fluids, multiphase flows and buoyancy-driven flows, among others. The developed open-source solver solves the Navier–Stokes set of equations and an advection-diffusion equation of a passive scalar, and incorporates particular features namely, special boundary conditions, a non-Newtonian viscosity model for blood and a pulsatile inflow law. In this way, simulations can be adapted to various patient specifications. Moreover, important WSS and LDL-based descriptors can be easily calculated in a further step by means of the post-processing software Paraview[27] to detect vulnerable parts of the vessel prone to develop atherosclerotic plaques. Comparing to other valuable open-source options like CRIMSON[28] and SimVascular,[29] our model can offer distinct advantages. Since OpenFOAM is widely used and a well-known software within the CFD community, end users can rely on the existing community to further modify and customize the provided code. Additionally, they can benefit from already implemented numerical schemes for spatial and temporal interpolations, as well as a wide range of system of equation solvers. Finally, our model includes special features for LDL transport simulations, such as a specific Robin boundary condition for the vessel wall.

The article is structured as follows. In Section 2, we introduce the numerical model, starting with the governing equations (Section 2.1) and details about special boundary conditions and the viscosity model used to recreate blood currents in arteries (Sections 2.2 and 2.3). After that, Section 2.4 gives specifics about the implementation in the OpenFOAM framework. Numerical experiments are explained in Section 3. The first two tests, described in Section 3.1, aim to validate the numerical model. These tests involve the classical lid-driven cavity with heat advection and a constricted tube simulating a stenosed artery. In the third simulation we compute the hemodynamics, LDL transport, and relevant descriptors of a coronary artery whose geometry is freely available (Section 3.2.1). Finally, the same approach is taken in Section 3.2.2,

where we test an artery obtained through segmentation from anonymized clinical patient data. Final remarks in Section 4 close the article.

2 | NUMERICAL MODEL

2.1 | Governing equations

The continuous model for fluid flow solution is the set of Navier–Stokes equations for an incompressible and transient flow with density ρ_f and dynamic viscosity μ_f,

$$\nabla \cdot \mathbf{u} = 0, \tag{1}$$

$$\frac{\partial \mathbf{u}}{\partial t} + \nabla \cdot (\mathbf{u}\mathbf{u}) = -\frac{1}{\rho_f}\nabla p' + \frac{1}{\rho_f}\nabla \cdot \boldsymbol{\tau}, \tag{2}$$

in $\Omega \in \mathbf{R}^d, t \in \left[t_0, T_f\right]$. Here, $\mathbf{u}(\mathbf{x}, t)$ is the velocity field ($\mathbf{x} = (x_l), l = 1, d$), d is the number of space dimensions, $p' = p - \rho_f g z$ is the dynamic pressure, g is the module of the gravity acceleration, z is the vertical coordinate, $\boldsymbol{\tau} = \mu_f \nabla^2 \mathbf{u}$ is the viscous stress tensor and $[t_0, T_f]$ is the time interval.

Low-density lipoproteins are assumed to be present in dissolved form in the blood current, and they are modeled as a passive non-reacting scalar (see e.g., Reference 5). Then, the equations system for flow solution (1) and (2) is coupled with the advection-diffusion equation, given in Equation (3),

$$\frac{\partial \phi}{\partial t} + \nabla \cdot (\mathbf{u}\phi) = K\nabla^2 \phi \ \text{ in } \Omega \ , t \in [t_0, T_f]. \tag{3}$$

Here, ϕ is the LDL concentration, K is the diffusivity of LDL in flowing blood and boundary conditions (see e.g., Reference 30) are

$$\phi = \overline{\phi}(\mathbf{x}, t) \ \text{ on } \Gamma_\phi^-, \tag{4}$$

$$\phi \mathbf{u} \cdot \mathbf{n}_b = \overline{\mathbf{q}}_\phi(\mathbf{x}, t) \cdot \mathbf{n}_b \ \text{ on } \Gamma_q^-, \tag{5}$$

being $\Gamma^- = \Gamma_\phi^- \cup \Gamma_q^-, \Gamma^- = \{\mathbf{x} \in \Gamma : (\mathbf{u} \cdot \mathbf{n}_b) \le 0\}$, with the initial condition

$$\phi(\mathbf{x}, t_0) = \overline{\phi}_0(\mathbf{x}) \ \text{ in } \Omega. \tag{6}$$

The domain Ω in $\mathbf{R}^d$ is bounded by $\Gamma = \Gamma^- + \Gamma^+$, and $\overline{\phi}$ and $\overline{\mathbf{q}}_\phi$ are known (the latter a vector) functions (from now on overline designates known values). We denote the inflow boundary by Γ^-, while $\Gamma^+ = \{\mathbf{x} \in \Gamma : (\mathbf{u} \cdot \mathbf{n}_b) > 0\}$ is the outflow boundary, and $\mathbf{n}_b$ is the outward unit normal to the boundary.

2.2 | Boundary conditions for blood flow problems

We normally distinguish three boundary conditions in simulations involving the computation of hemodynamics in arteries.

First, at the inflow boundary, we consider that the normal gradient of pressure is zero $\left(\frac{\partial p}{\partial \mathbf{n}_b} = 0\right)$, and that the LDL concentration is constant ($\phi = \overline{\phi}$). Moreover, blood flow is assumed pulsatile with a mean flow rate computed using,[31]

$$\overline{q}_{\text{in}} = 1.43D^{2.55}. \tag{7}$$

In Equation (7), units of $\overline{q}_{\text{in}}$ are m^3/s, $D = 2\sqrt{A/\pi}$ is the artery equivalent inlet diameter (in meters), and A is the inlet surface area. Thus, inlet velocity magnitude is defined as follows,

$$u(t) = \overline{U}\left[1 + \sum_{k=1}^{\infty}\left(a_k \cos\left(\frac{2\pi k}{T_c}t\right) + b_k \sin\left(\frac{2\pi k}{T_c}t\right)\right)\right], \tag{8}$$

where $\overline{U} = \overline{q}_{in}/A$ is the time-averaged inlet velocity, terms in brackets represent the Fourier series describing a human heartbeat waveform, and T_c is the duration of a complete cardiac cycle. In Appendix A, we present the values of amplitudes a_k, b_k for two different waveforms obtained from References 32 and 33.

Second, regarding outlet boundaries, we differentiate arteries with and without a bifurcation. For arteries consisting of a single branch, we impose that the normal gradients of velocity and LDL concentration are zero, and that the relative pressure is also zero. On the other hand, for arteries with a bifurcation (see example in Figure 7) we impose the velocity at one outlet according to next equation valid for coronary arteries (see details in Reference 31),

$$u_1(t) = u(t)\frac{\left(\frac{D}{D_1}\right)^2}{1 + \left(\frac{D_2}{D_1}\right)^{2.27}}, \tag{9}$$

where subscripts 1 and 2 refer to both outlets situated at the end of the branches (see Figure 7). Moreover, at outlet one we establish that normal gradients of pressure and LDL concentration are zero. Boundary conditions at outlet 2 are the same as for the outlet in arteries without bifurcation.

Finally, at walls, we assume no-slip conditions ($\mathbf{u} = 0$) and that the normal gradient of pressure is zero. In addition, LDL concentration in the arterial wall is determined by next Robin boundary condition,

$$\phi_w V_w - K\frac{\partial \phi_w}{\partial \mathbf{n}_b} = M_w \phi_w, \tag{10}$$

which represents a mass conservation and states that the amount of LDL passing through a vessel wall is determined as the difference between the amount carried to the vessel wall by a filtration flow and the amount which diffuses back to the mainstream.[34] In Equation (10), ϕ_w is the LDL concentration at the arterial wall, V_w is the water filtration velocity, and M_w is the overall mass transfer coefficient.

2.3 | Blood viscosity model

Although the deformability of single red blood cells has been linked to the pathogenesis of several diseases such as malaria in previous studies.[35,36] In this work, blood as a whole is assumed to be an incompressible and non-Newtonian fluid with density $\rho_f = 1060$ kg/m^3. We adopt the Casson fluid model,[37] which has been employed in several previous works involving blood flows (see e.g., References 38 and 39). Hence, the viscous stress tensor is computed as,

$$\frac{\tau_{ij}}{\rho_f} = v_f \dot{\gamma}_{ij} = v_f\left(\frac{\partial u_i}{\partial x_j} + \frac{\partial u_j}{\partial x_i}\right), \tag{11}$$

$$v_f = v_f(|\dot{\gamma}|) = \left(\sqrt{\frac{\tau_0}{|\dot{\gamma}|}} + \sqrt{m}\right)^2, \quad v_{min} \leq v_f \leq v_{max}, \tag{12}$$

where v_f is de kinematic viscosity (m^2/s), $\dot{\gamma}$ is the shear rate (1/s), $\tau_0 = 3.77 \times 10^{-6}$ m^2/s^2 is the threshold stress, $m = 2.83 \times 10^{-6}$ m^2/s is the flow consistency index and $v_{min} = 2.83 \times 10^{-6}$ m^2/s, $v_{max} = 6.604 \times 10^{-5}$ m^2/s are the minimum and maximum viscosity allowed, respectively. Previous parameters represent the rheology of blood at 37°C, and were obtained from Section 4.8 and fig. 4.4 of Reference 40.

2.4 | Implementation in the OpenFOAM framework

As previously stated, OpenFOAM is an open-source library of C++ codes developed to solve problems in the field of the CFD. The solver introduced in this work, is derived from *pisoFOAM*, designed to calculate the solution of Equations (1)

and (2) by using the PISO algorithm[41] (pressure-implicit with splitting of operators). This solver has been properly modified by incorporating the solution of Equation (3), employing the non-stationary velocity field obtained in the hemodynamics computation.

OpenFOAM also includes several numerical schemes for time discretization and for gradients, divergence, and Laplacian terms integration. For all numerical experiments in this work, an Euler implicit time scheme is used for temporal integration, whereas gradients are calculated by linearly interpolating the field to the cell's faces. Different strategies of interpolation are adopted for divergence terms. On one hand, viscous terms are integrated using a linear interpolation, and, on the other hand, advective terms are computed by using an upwind second-order interpolation. Finally, for Laplacian terms integration, a linear interpolation with a non-orthogonal correction is used.

Concerning boundaries, Dirichlet and Neumann conditions were already implemented in OpenFOAM as wall or fixed-gradient conditions. However, the conditions specified by Equations (8)–(10) are time-dependent or of Robin-type. Therefore, they should be manually prescribed using the user-coded conditions named *codedFixedValue* and *codedMixed*. Further, special care must be taken when inlet velocities given by Equation (8) adopt negative values (see as example Figure A1). In that case, boundary conditions for LDL concentration ϕ should be customized to adapt them to the velocity. The flow chart presented in Figure 1 illustrates the structure of the algorithm and the prescribed boundary conditions. Initially, the artery's geometry and blood's physical parameters are read. Then, for each time-step, the code calculates the inlet velocity according to Equation (8). At this stage, four scenarios can occur: (a) the vessel is a single branch with a positive inlet velocity, (b) the vessel has a bifurcation and the inlet velocity is positive, (c) the vessel is a single branch with negative inlet velocity, and (d) the vessel has a bifurcation and the inlet velocity is negative. Boundary conditions for cases (a) and (b) are detailed in Section 2.2. However, in cases (c) and (d), inlets become outlets and vice-versa. Therefore, boundary conditions for ϕ need to be switched, as shown in Figure 1. Subsequently, hemodynamics is computed, updating the pressure and velocity fields. Finally, the advection-diffusion Equation (3) for LDL concentration is solved by using the updated velocity field. The procedure is repeated until the final time is reached.

3 | RESULTS AND DISCUSSION

3.1 | Validation tests

3.1.1 | Lid-driven cavity with heat transport

The first test reproduces the classical lid-driven cavity benchmark, whose layout is shown in Figure 2. It consists in a closed two-dimensional squared cavity with side length $H = 1$ m where the upper lid has a constant velocity $\mathbf{u} = (U, 0) = (1, 0)$ m/s. Moreover, in this case, the moving lid is heated, and maintains a constant temperature of $T = 1$ K throughout the entire simulation. The remaining boundaries have no-slip conditions ($\mathbf{u} = 0$), and the lower wall maintains a constant temperature $T = 0$ K. Heat transfer is solved with advection-diffusion equation (3), where $\phi = T$ in this case and thermal diffusivity is $K = \frac{1}{\text{Re} \cdot \text{Pr}}$, being Re and Pr the Reynolds and Prandtl numbers, respectively. On the other hand, the non-dimensional term Gr/Re^2 (where Gr is the Grashof number) provides a measure of the relative importance of buoyancy-driven natural convection compared to forced convection induced by the lid. Then, if $\text{Gr}/\text{Re}^2 \ll 1$, the buoyancy effect is negligible, and the set of Equations (1) and (2) can be used to solve the hydrodynamics in the cavity.

To validate the proposed numerical model we replicate three of the experiments performed in Reference 42. These tests differ by the employed kinematic viscosity* and have, respectively, $\text{Re} = \frac{UH}{\nu_f} = 400$, $\text{Re} = 1000$ and $\text{Re} = 3000$. In all cases $\text{Pr} = 0.71$ and $\text{Gr} = 100$, therefore, condition $\text{Gr}/\text{Re}^2 \ll 1$ is fulfilled. Moreover, mesh discretization is set as $\Delta x = \Delta y = 1/256$ m, whereas $\Delta t = 2.5 \times 10^{-3}$ s. Once simulations are run until steady-state, velocity and temperature fields are measured and compared with outputs of Reference 42. Figures 3 and 4 show these comparisons, where dashed lines represent current outputs and solid lines are numerics of Reference 42. As can be noted, current results for $\text{Re} = 400$ are almost identical to outputs in Reference 42 (see Figures 3A,D and 4A). Otherwise, slight deviations appear in the temperature profile for $\text{Re} = 1000$ (see Figure 4C at $y \approx 0.95$ m and Figure 4D at $y \approx 0.4$ m), and in the horizontal velocity profile for $\text{Re} = 3000$ (see Figure 3C). Nevertheless, despite these small differences, the present numerical model accurately reproduces hydrodynamics of the problem, in addition to the temperature distribution given by the solution of the advection-diffusion equation.
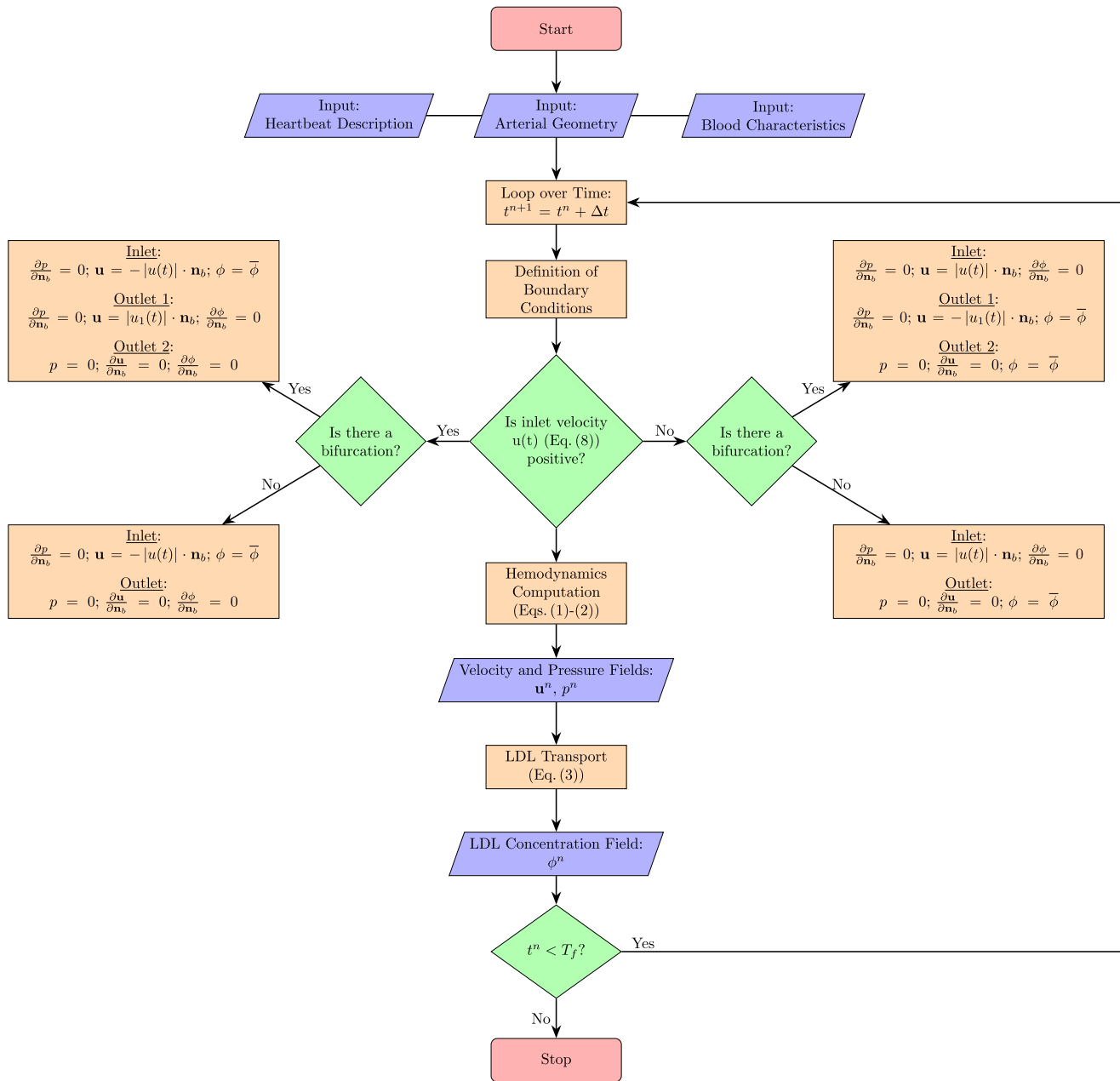
FIGURE 1   Flow chart of the numerical model implemented in OpenFOAM.

3.1.2 | Constricted tube

As a second benchmark test, we reproduce one of the laboratory experiments described in Reference 43. This test involves a tube with a diameter of $D = 0.0508$ m and a 75% area reduction to simulate a stenosed artery, as illustrated in Figure 5. Regarding the boundary conditions, we assume that the walls are no-slip, while the inlet and outlet are positioned at the left and right section of the tube, respectively. Although the geometry is axisymmetric, we have employed a three-dimensional grid with an average cell size[†] of $\delta = 9.32 \times 10^{-4}$ m. The reason for this is to use similar boundary conditions to those we will use for real arteries. The fluid used is a mixture of water and glycerol, with a kinematic viscosity of $\nu_f = 1.2 \times 10^{-5}$ m^2/s. It enters the tube with a mean inlet velocity of $\overline{U} = 0.118$ m/s, resulting in a Reynolds number of $\mathrm{Re} = \frac{\overline{U}D}{\nu_f} = 500$. We have run the simulation for 20 s to reach the steady state.

$$\mathbf{u} = (U, 0), \ T = 1$$

$$\mathbf{u} = 0, \ \frac{\partial T}{\partial \mathbf{n}_b} = 0$$

$$\mathbf{u} = 0, \ \frac{\partial T}{\partial \mathbf{n}_b} = 0$$
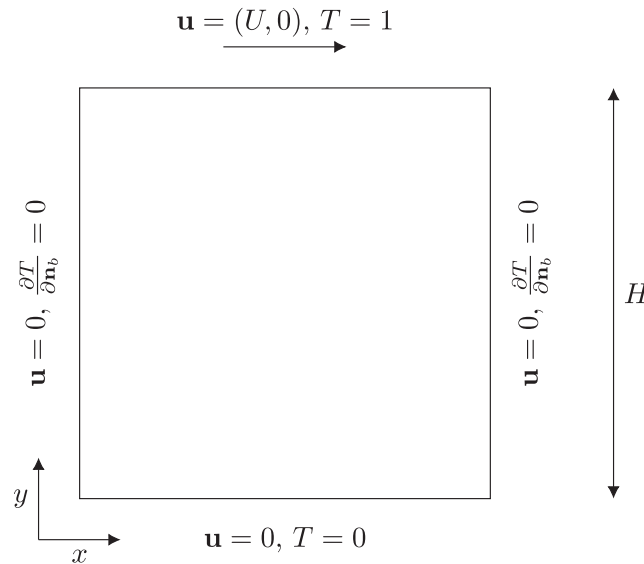
$$H$$

$$y$$

$$x$$

$$\mathbf{u} = 0, \ T = 0$$

FIGURE 2 Schematic diagram of a classical lid-driven cavity benchmark test with detailed dimensions and boundary conditions.

Numerical results are depicted in Figure 6, where we show the non-dimensional axial velocity profile $U/\overline{U}$ at different distances X from the throat of the constriction. Experimental measurements[43] and results obtained with a direct numerical simulation of the problem[44] are also superimposed in Figure 6. As can be seen, our numerics (solid lines) at the vicinity of the tube centerline are almost identical to experimental measurements and results of Varghese et al. for all cases. On the other hand, slight differences can be appreciated in the region between the tube axis and the wall, where our numerical results for $X/D = 1$, 4 and 6 fall between the outputs obtained from the two reference studies. For $X/D = 2.5$, differences are more evident, resulting in a mean error of 1.6% respect to experimental measurements. These results demonstrate the capability of our numerical model to accurately resolve the hydrodynamics in geometries featuring constrictions, akin to stenosed arteries, which are one of the targets of the presented numerical model.

3.2 | Hemodynamics solution and LDL transport in coronary arteries

3.2.1 | Case 1

In this section, we calculate hemodynamics, LDL concentration, and WSS of the artery shown in Figure 7. The grid for this artery is freely available for the OpenFOAM framework in Reference 45. The main branch of the vessel has an inlet diameter of 2.1 mm approximately, after which the artery bifurcates into two secondary branches with diameters of 1.6 mm and 1.4 mm. The employed grid has an average cell size $\delta \approx 8 \times 10^{-2}$ mm (see detail in Figure 7). To compute hemodynamics and LDL advection, blood is assumed incompressible with the Casson viscosity model outlined in Section 2.3, and LDL diffusivity is $K = 5.983 \times 10^{-12}$ m²/s.[34] Boundary conditions are the same as those explained in Section 2.2, being the LDL concentration at inlet $\overline{\phi} = 100$ mg/dL (normal value in humans). On the other hand, the vessel wall is considered undamaged with a water filtration velocity $V_w = 4 \times 10^{-8}$ m/s (see Reference 34 and references therein), and the overall mass transfer coefficient M_w is commonly assumed negligible.[5] Inflow is simulated using the waveform 2 described in Appendix A, assuming a cardiac cycle of $T_c = 0.8$ s. The test starts by considering that blood is at rest and that LDL concentration is zero in the whole domain, then the simulation is run until $t = 6$ s. Outcomes of LDL concentration and WSS[‡] τ_w at the final time-step are shown in Figure 8. The highest values of WSS are located in the bifurcation region as expected, while maximum and minimum LDL concentrations are found at those wall parts nearby zones with high and low velocity values, respectively. However, near-wall hemodynamics is usually evaluated in terms of descriptors as, for example, the time averaged wall shear stress (TAWSS), the oscillatory shear index (OSI) and the relative residence time (RRT) (see e.g., Reference 46 and references therein), which are defined as follows,

$$\text{TAWSS} = \frac{1}{T_c} \int_0^{T_c} |\tau_w| \, \mathrm{d}t, \tag{13}$$
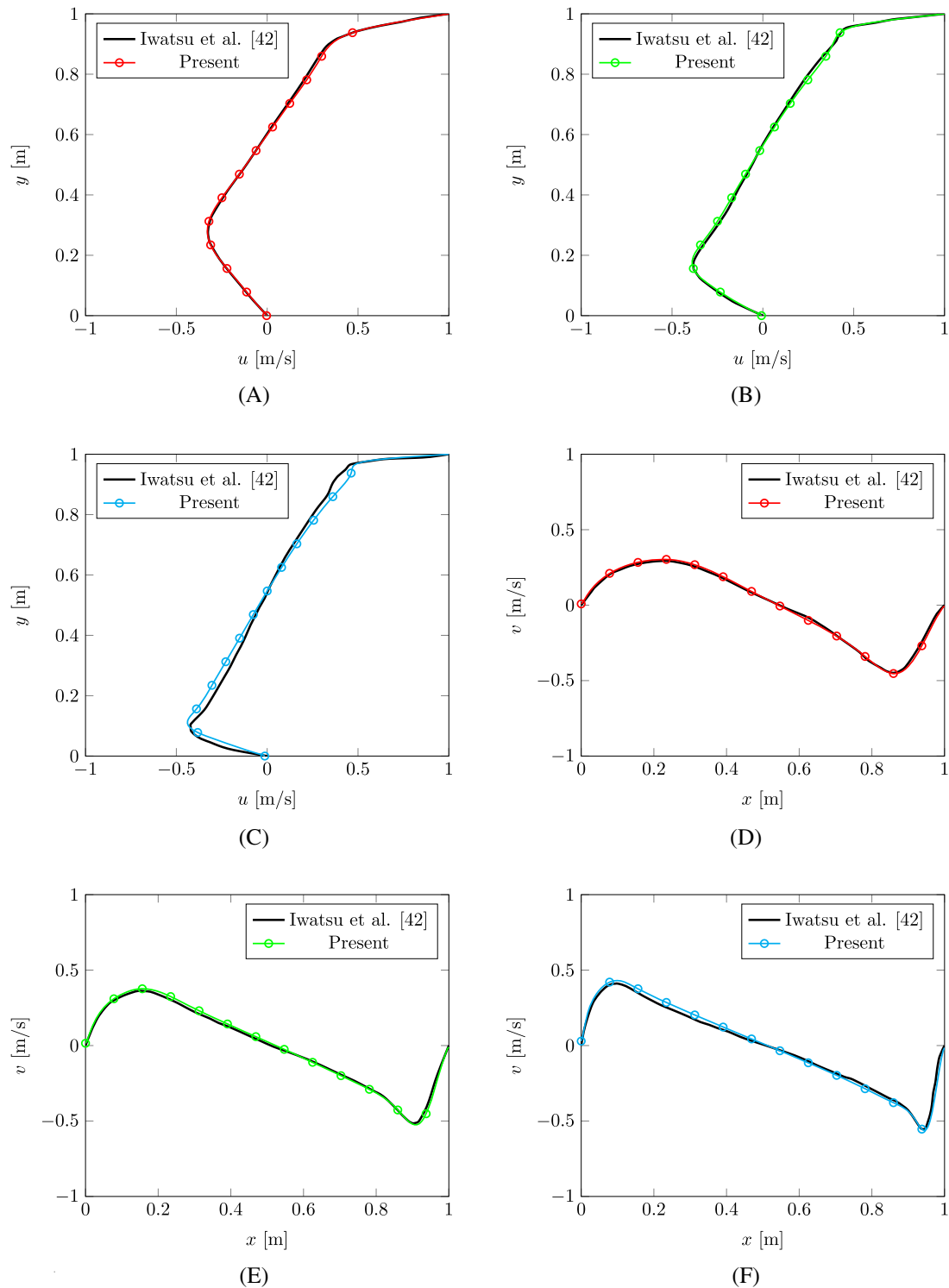
FIGURE 3 Lid-driven cavity: Horizontal velocity profiles (u) at $x = 0.5$ m, and vertical velocity profiles (v) at $y = 0.5$ m for several Reynolds numbers. Comparison between outputs shown in Reference 42 and present results. (A) Horizontal velocity profile at $x = 0.5$ m, Re = 400. (B) Horizontal velocity profile at $x = 0.5$ m, Re = 1000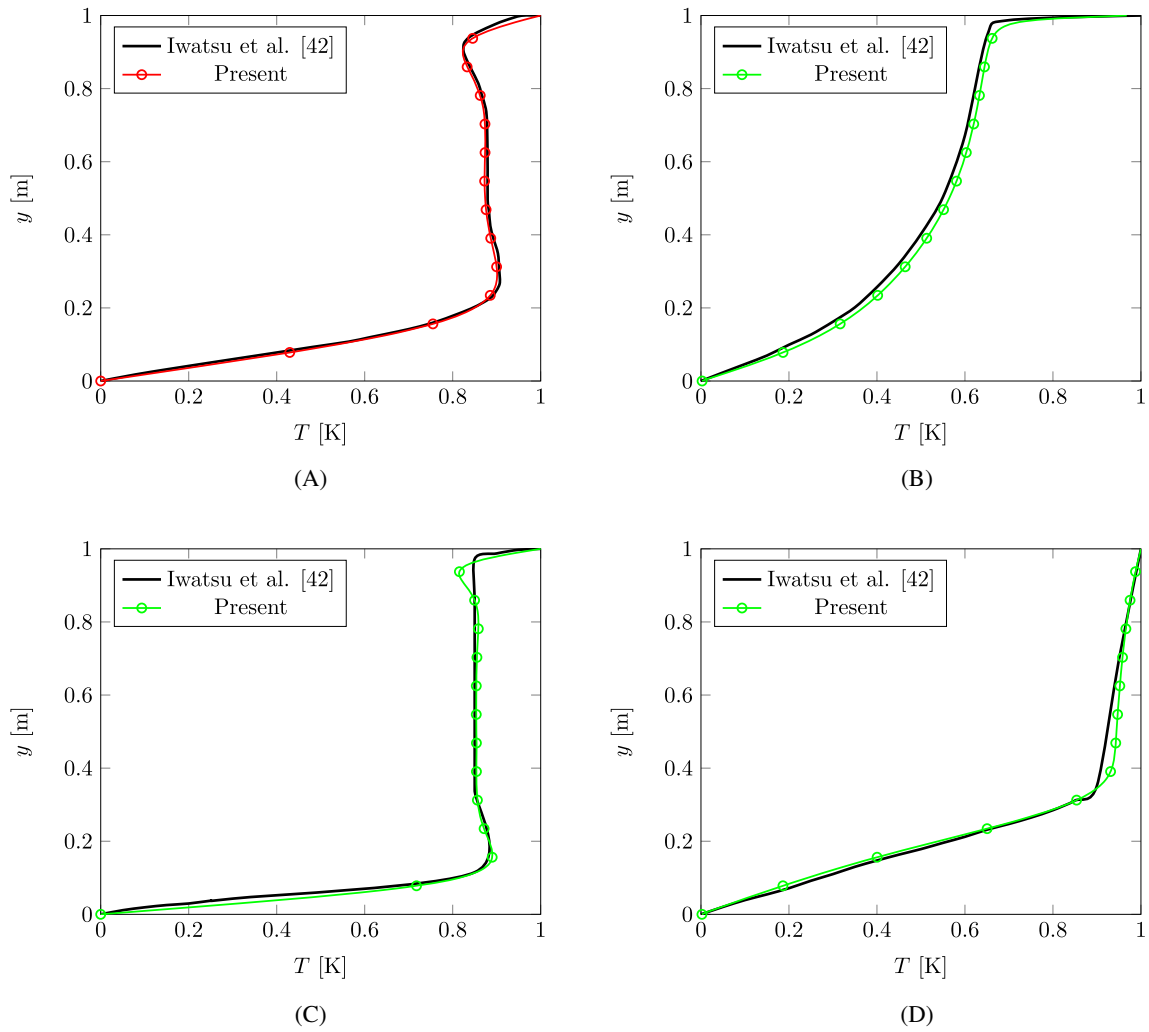. (C) Horizontal velocity profile at $x = 0.5$ m, Re = 3000. (D) Vertical velocity profile at $y = 0.5$ m, Re = 400. (E) Vertical velocity profile at $y = 0.5$ m, Re = 1000. (F) Vertical velocity profile at $y = 0.5$ m, Re = 3000.

FIGURE 4 Lid-driven cavity: Temperature profiles for several Reynolds numbers. Comparison between outputs shown in Reference 42 and present results. (A) Temperature at $x = 0.5$, Re = 400. (B) Temperature at $x = 0$, Re = 1000. (C) Temperature at $x = 0.5$, Re = 1000. (D) Temperature at $x = 1$, Re = 1000.
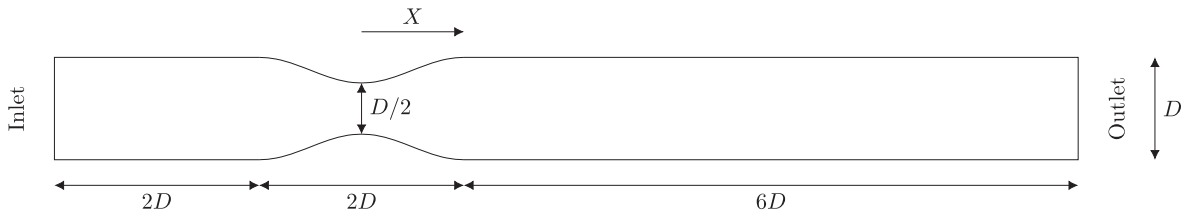

FIGURE 5 Constricted tube: Layout and boundary conditions.

$$\text{OSI} = \frac{1}{2}\left[1 - \left(\frac{\left|\int_0^{T_c} \tau_w \, dt\right|}{\int_0^{T_c} |\tau_w| \, dt}\right)\right], \tag{14}$$

$$\text{RRT} = \frac{T_c}{\left|\int_0^{T_c} \tau_w \, dt\right|} = \frac{1}{\text{TAWSS} \cdot (1 - 2 \cdot \text{OSI})}. \tag{15}$$
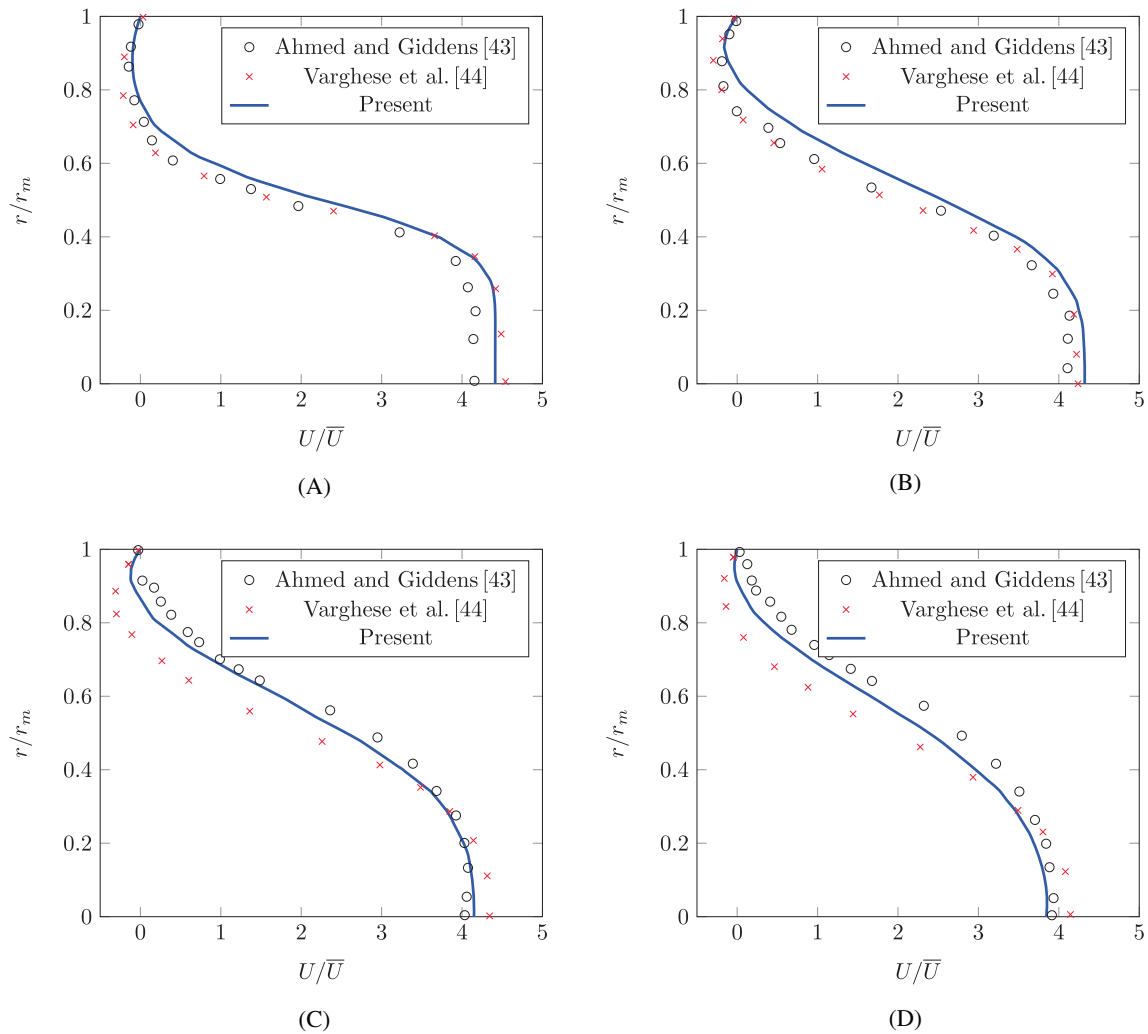
FIGURE 6 Constricted tube: Non-dimensional axial velocity profiles $U/\overline{U}$ at different distances X from the throat of the constriction. In these figures, r is the radial coordinate measured from the centerline of the tube, and r_m is the local radius of the section. (A) $X/D = 1$. (B) $X/D = 2.5$. (C) $X/D = 4$. (D) $X/D = 6$.
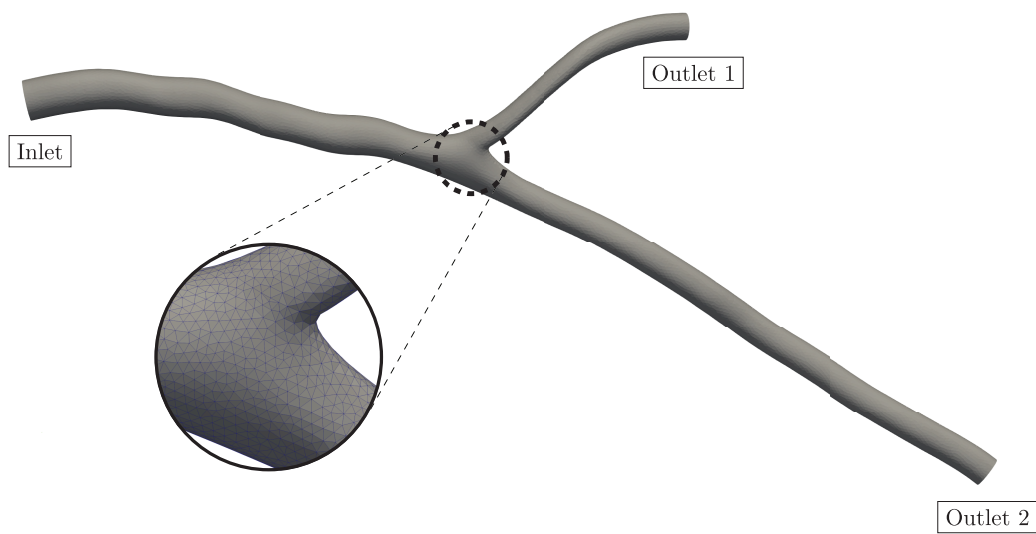

FIGURE 7 Coronary artery used for Case 1 showing the geometry, mesh discretization at the bifurcation and boundaries—1 inlet and 2 outlet points.
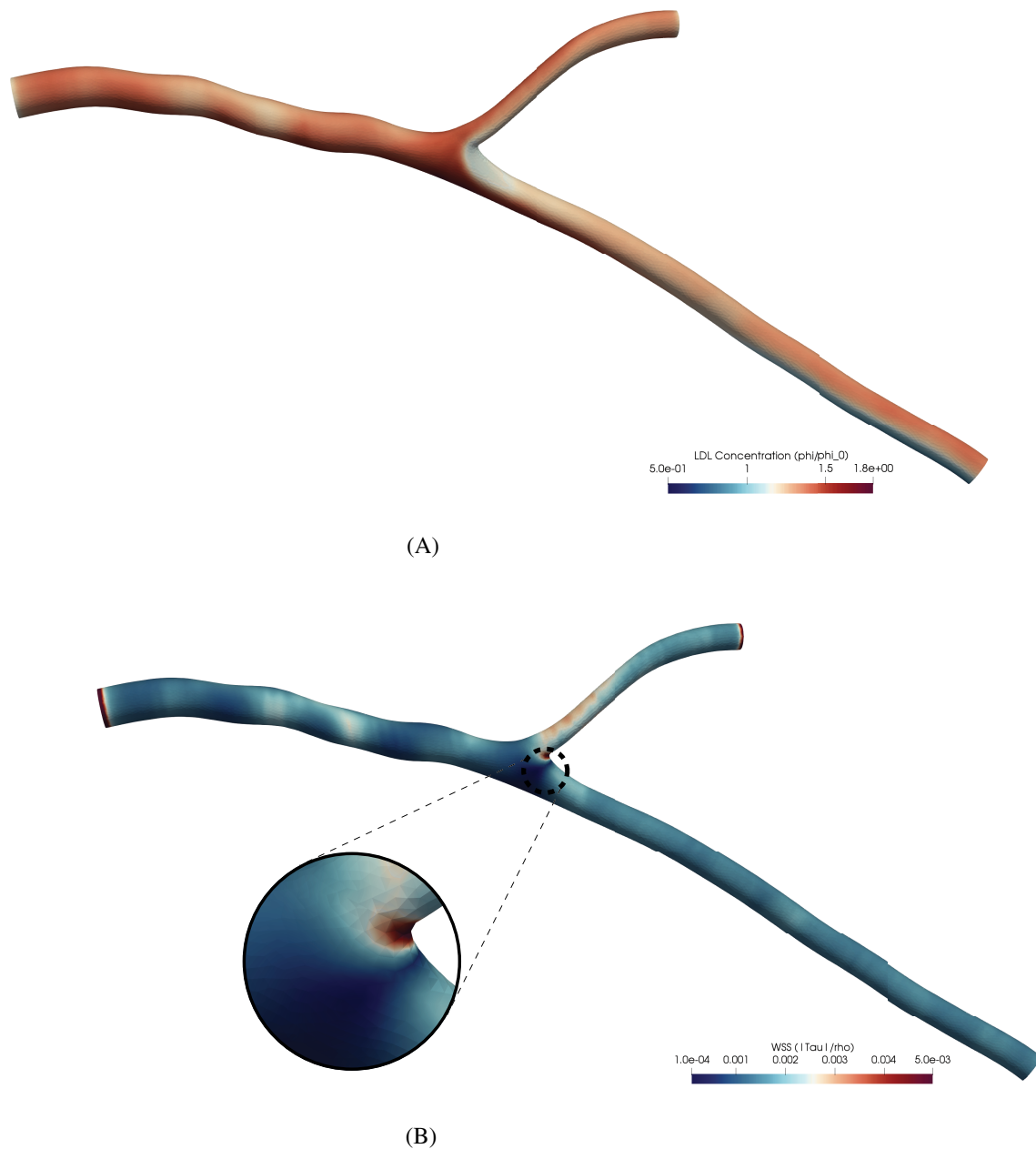
FIGURE 8 Coronary artery test (Case 1): Numerical outcomes of LDL concentration and wall shear stress at $t = 6$ s. Results of LDL are represented as the ratio between current and inlet concentration, and units of WSS are m^2/s^2. (A) LDL concentration ($\phi/\overline{\phi}$). (B) Wall shear stress (τ_w/ρ_f).

Furthermore, according to Reference 47, these indicators are nearly insensitive to the use of fluid-structure interaction (FSI) or rigid-wall models in the simulation.

Severe atherosclerotic plaques typically develop and grow in areas with low WSS and high LDL concentration (see e.g., References 8,20, and 48). Therefore, TAWSS, OSI, and RRT were calculated for time interval $t \in [4.8, 5.6]$ s (seventh simulated cardiac cycle) and, after pooled, the 20th percentile value of TAWSS and 80th percentile values of OSI, RRT and LDL were identified following Reference 5. Thus, luminal surface portions included in TAWSS20, OSI80 and RRT80 have low or oscillating WSS values, which means that the region has a high residence time and that it is prone to house LDL deposits. In addition, wall portions included in LDL80 present a high LDL concentration. Figure 9 depicts parts of the vessel's wall included in descriptors TAWSS20 and LDL80, denoting that it is unlikely that atherosclerotic plaques develop at secondary branches in this case. Otherwise, main branch exhibits some small zones at risk co-localized in both
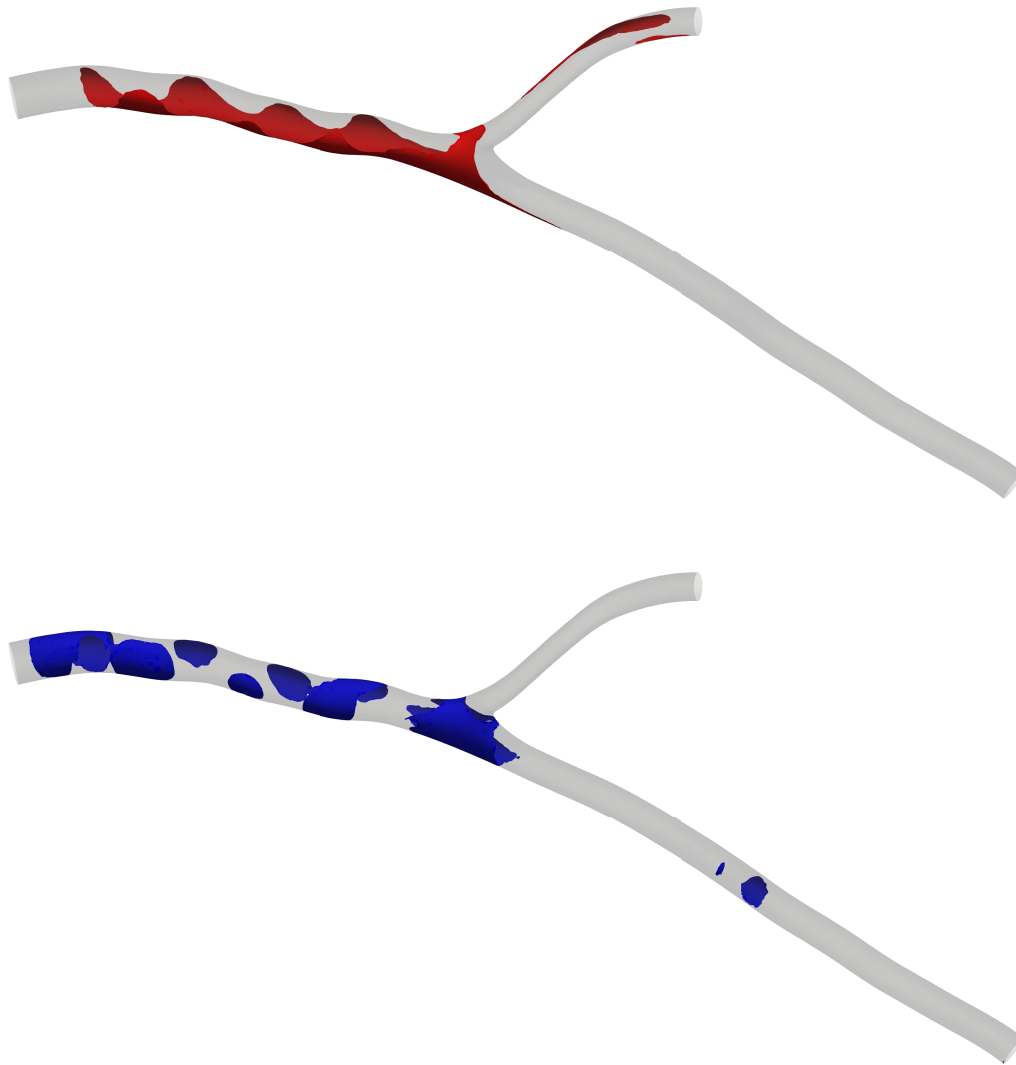
FIGURE 9 Coronary artery test (Case 1): Portions of the luminal surface included descriptors LDL80 (above, colored in red) and TAWSS20 (below, colored in blue). Both descriptors are present at the bifurcation, being this zone a candidate to develop atherosclerotic plaques.

descriptors. However, consistent with in-vivo observations (see e.g., References 49 and 50), the vicinity of the bifurcation appears to be the most susceptible region, as it exhibits a well-defined area with both high LDL concentration and low TAWSS. Therefore, our numerical results suggest that the bifurcation's vicinity should be monitored closely for early detection of atherosclerotic plaque formation (or progression).

Now, we evaluate effects of viscosity and mean velocity on the LDL concentration and WSS values. To this end, we have performed two additional simulations varying the blood viscosity model and the inlet flow rate. In the first supplementary test, we simulate the effect of a blood-viscosity-reducing drug by adjusting the coefficients of the Casson model. Results of WSS and LDL concentration under these conditions are depicted in Figure 10, which shows, as expected, reduced WSS values (Figure 10B) due to the stress tensor's dependence on viscosity (see Equation 11). Nevertheless, LDL concentration at walls (see Figure 10A) is similar to values presented in Figure 8A. In the second test we simulate a physical activity by setting the inlet flow rate as double ($\overline{q}_{in} = 2.86D^{2.55}$) and the cardiac cycle as $T_c = 0.4$ s. The outputs are displayed in Figure 11. As in the previous case, the LDL concentration (Figure 11a) is very similar to the original test. However, the WSS values have increased considerably due to the higher near-wall blood velocity. Thus, the significance of WSS in atherosclerosis is evinced in these tests: while transient phases of high WSS, for example, by means of physical activity, can prevent the genesis of atherosclerotic plaques via mechanotransduction pathways,[51] if plaques are already formed,
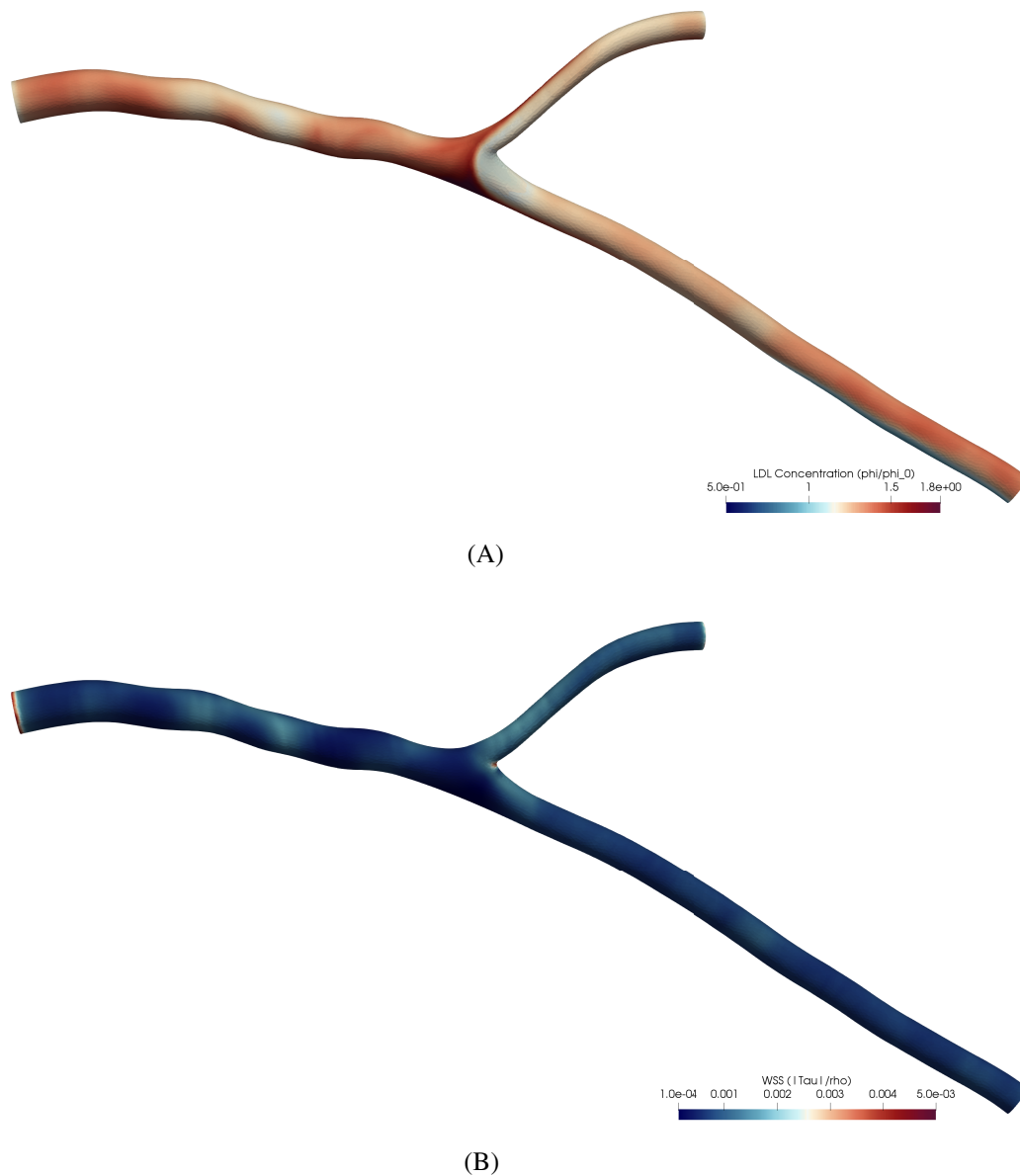
FIGURE 10 Coronary artery test (Case 1) with low viscosity blood: Numerical outcomes of LDL concentration and wall shear stress at $t = 6$ s. Results of LDL are represented as the ratio between current and inlet concentration, and units of WSS are m^2/s^2. (A) LDL concentration ($\phi/\overline{\phi}$). (B) Wall shear stress (τ_w/ρ_f).

high WSS can promote plaque vulnerability and rupture. Then, in this situation, it is desirable the reduction of WSS by artificially changing the blood's physical properties.

3.2.2 | Case 2

In this case, we study an artery obtained from a computed tomography coronary angiogram (CTCA) of an anonymized clinical patient. The artery is shown in Figure 12, and has a main branch (proximal left anterior descending artery coronary artery) of 3.27 mm diameter, and 16 mm length approximately, while secondary branches (mid left anterior descending and first diagonal branch) have 1.83 mm diameter, 15 mm, length and 1.67 mm diameter, 18 mm length, respectively. The original CTCA dataset was supplied in DICOM format, and we computed the finite volume mesh entirely using open-source software. The procedure can be outlined as follows:
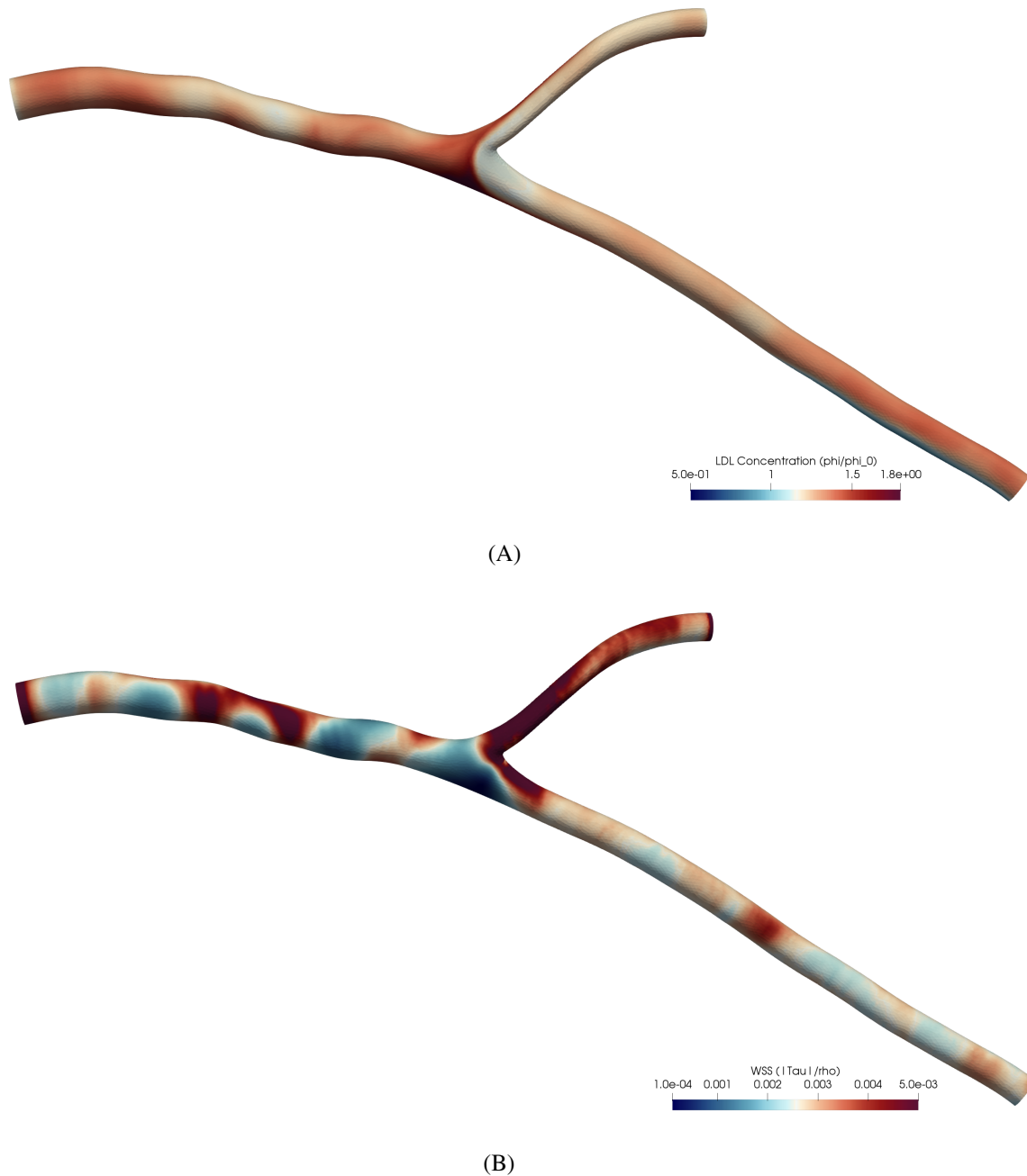
FIGURE 11   Coronary artery test (Case 1) with a high blood flow rate: Results of LDL concentration and shear stress at walls at $t = 3$ s. Results of LDL are represented as the ratio between current and inlet concentration, and units of WSS are m^2/s^2. (A) LDL concentration ($\phi/\overline{\phi}$). (B) Wall shear stress (τ_w/ρ_f).

1. Segmentation is performed using the software 3DSlicer[52] (http://www.slicer.org/). With this tool, we select and extract the artery, resulting in an STL file that contains the geometry (see snapshots in Figure 12A).
2. Spatial discretization is performed using Salome Platform (https://www.salome-platform.org/), which includes several mesh generation algorithms. In this case, we discretized the geometry using tetrahedrons and prisms (see Figure 12B), thus obtaining a file in UNV format.
3. Import the mesh file to OpenFOAM with command *IdeasUnvToFoam*.

The resulting grid has 215,853 nodes and $\delta \approx 7.291 \times 10^{-2}$ mm. Additionally, the thickness of the first element layer is 4.81×10^{-3} mm to improve the convergence of near-wall LDL transport computation.[53] On the other hand, initial and
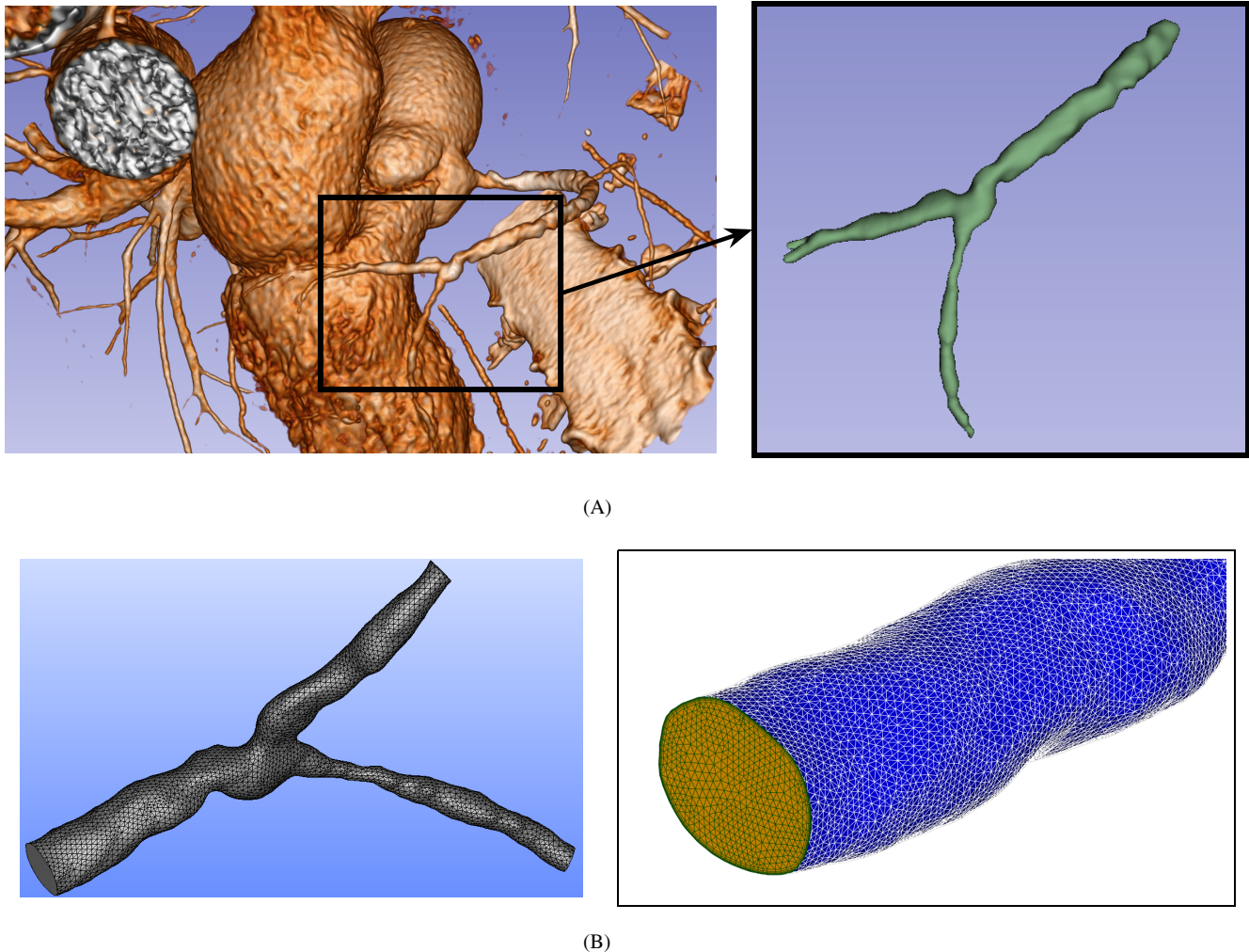
(A)

(B)

FIGURE 12 Coronary artery test (Case 2): Snapshots of the artery mesh generation. Segmentation process is performed with 3DSlicer and finite volume discretization is done by using Salome. (A) Segmentation process. (B) Spatial discretization.

boundary conditions are the same as in the first test of previous section. A total of six seconds have been computed in parallel using MPI (already integrated in OpenFOAM). Figure 13 depicts results of LDL concentration and WSS values at $t = 5.2$ s, showing a peak of stress in one of the branches, which seems to have stenosis. This is caused by the high velocity of the blood when passing through the narrowed zone. In addition, WSS and LDL indicators have been calculated for the seventh cardiac cycle ($t \in [4.8, 5.6]$ s) and are displayed in Figure 14. In contrast to the preceding simulation in Section 3.2.1, we observed that at the bifurcation, the sections of the vessel wall exhibiting elevated LDL concentrations do not align with those experiencing low TAWSS. This discrepancy arises from the vessel geometry in this particular zone. Notably, as illustrated by the streamlines in Figure 13C, there are specific parts of the vessel with a nearly stagnant blood flow which prevents the LDL introduced at the inlet from reaching its luminal surface (Figure 13A). This idle blood flow also results in remarkably low WSS values (see Figure 13B). Furthermore, stagnant zones induce the flow to stick to the outer face of the bifurcation, yielding the outcomes depicted in Figures 13 and 14, where a notable concentration of LDL is observed at the bifurcation along with elevated WSS values. Nevertheless, this test does unveil a dangerous region downstream of the stenosed segment of the daughter branch, characterized by a low TAWSS. Comparable findings were observed in previous studies involving stenosed arteries, as documented in Reference 54. Besides, this region also exhibits high LDL concentrations that, in conjunction with reduced TAWSS values, may foster the progression of an existing plaque or even the initiation of a new one. Consequently, close monitoring of this region is imperative.
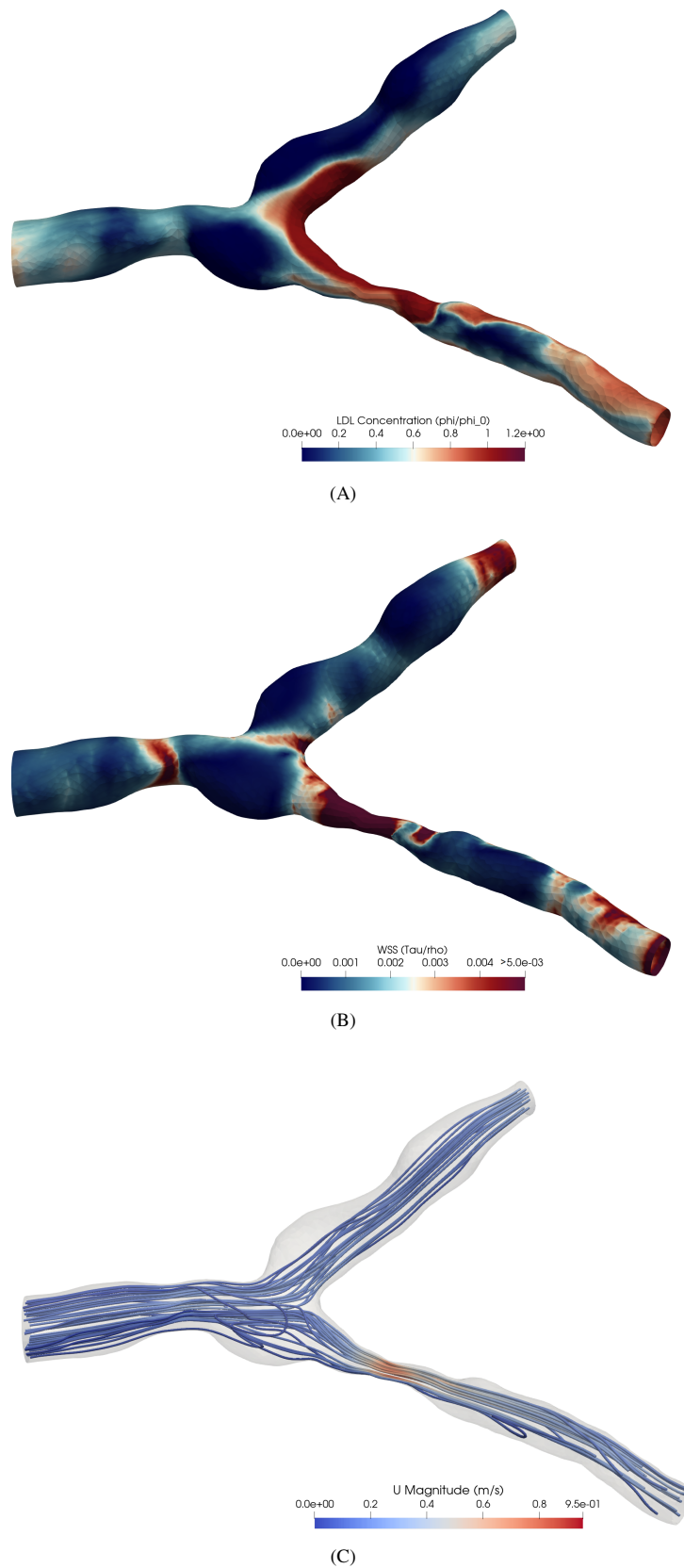
FIGURE 13 Coronary artery test (Case 2): Results at $t = 5.2$ s of (A) LDL concentration, (B) shear stress at walls, and (C) streamlines colored according to the velocity magnitude. Results of LDL are represented as the ratio between current and inlet concentration, and units of WSS are m^2/s^2. (A) LDL concentration ($\phi/\overline{\phi}$). (B) Wall shear stress (τ_w/ρ_f). (C) Streamlines.
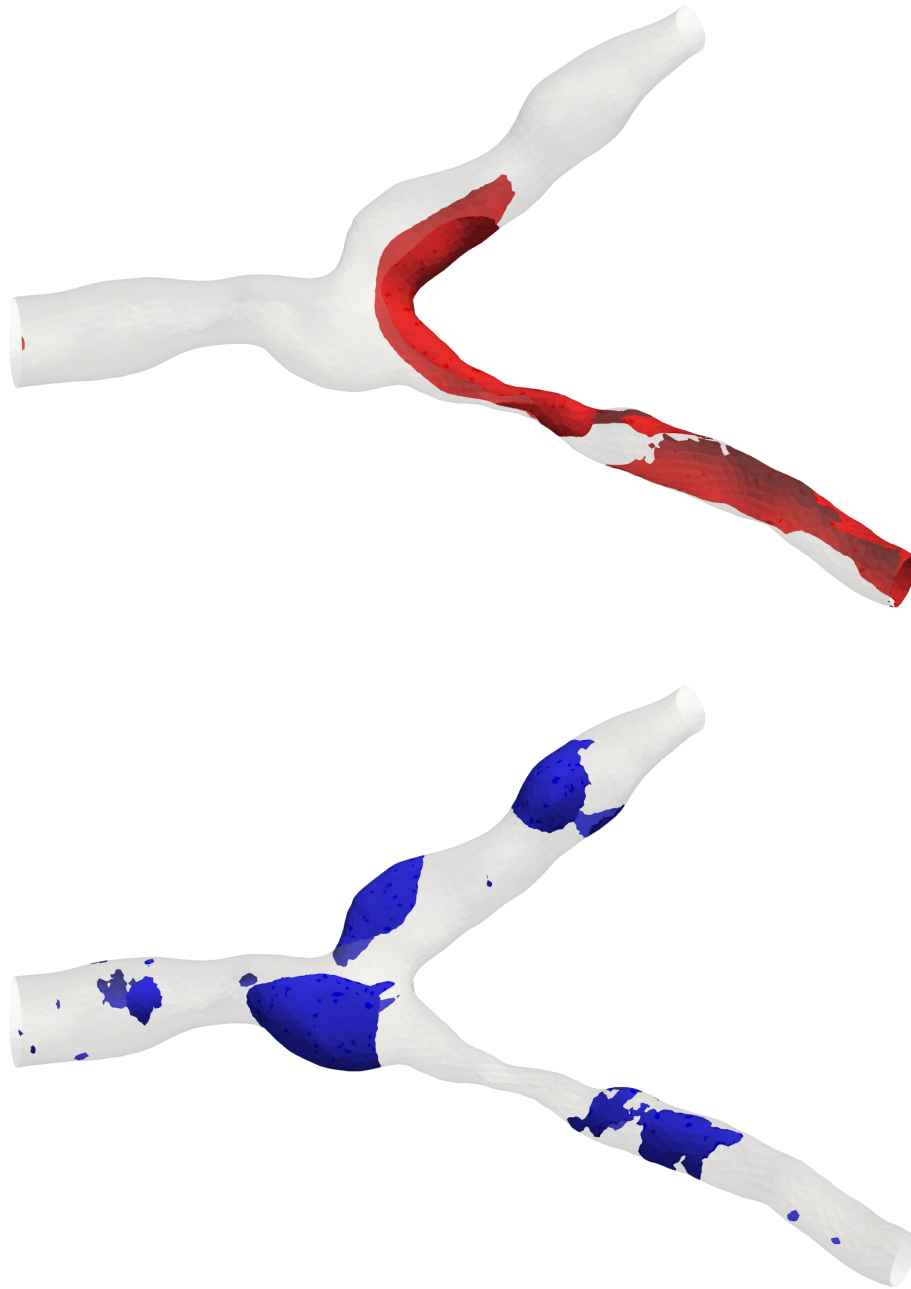
FIGURE 14   Coronary artery test (Case 2): Portions of the luminal surface included in the descriptors LDL80 (above, colored in red) and TAWSS20 (below, colored in blue). Both descriptors are present downstream the stenosed section of the lower daughter branch.

4 | CONCLUDING REMARKS

The numerical model presented in this study has been developed within the OpenFOAM framework and integrates the solution of an advection-diffusion equation to the preexisting solver *pisoFoam*. The algorithm can compute the convective transport of a passive scalar driven by a transient fluid, whose dynamics is also solved in time. It incorporates some features to accurately simulate blood flows, and LDL transfer in arteries. These features include a pulsatile inflow boundary condition emulating heartbeats, a realistic wall condition for LDL and a non-Newtonian viscosity model, among others.

The model was first validated by reproducing the lid-driven cavity test with heat transport. Numerics from hydrodynamics solution and heat distribution match almost perfectly with existing outcomes of Reference 42 for Re = 400, whereas deviations are very small for Re = 1000 and Re = 3000. Moreover, we have replicated one of the laboratory experiments performed in Reference 43. This test involves a constricted tube that emulates a 75% stenosed artery. Again, the

velocity outputs obtained from the hydrodynamics solution for Re = 500 align very well with experimental measurements. These results indicate that the numerical schemes selected, as detailed in Section 2.4, are appropriate and yield accurate results for the hydrodynamics and the passive scalar distribution. In the third and fourth experiments, we simulate the blood flow and LDL transport through a section of an idealized coronary artery with a bifurcation and through a real vessel. In these cases, results are evaluated by the computation of some descriptors revealing those parts of the vessel's wall where TAWSS is low and LDL concentration is high, being these ideal conditions for the emergence of atherosclerotic plaques. Based on our numerical results, we found that the most susceptible parts of the artery are the bifurcation and/or areas downstream of stenosed artery segments, which is in line with in-vivo observations. Numerical experiments also reveal that patient-specific simulations are indispensable in the study of atherosclerosis. For example, supplementary tests featuring high blood velocity and low viscosity have shown that WSS is distinctly influenced by the characteristics of blood flow and viscosity. Furthermore, the geometry and morphology of the artery determine the localization of regions susceptible to atherosclerotic plaque development, as demonstrated by differences observed in the two tested arteries.

It is worth noting that complex blood flow simulations in arteries remain of high interest to the scientific community. The presented numerical tool is designed to cater not only to seasoned researchers and experts in cardiovascular diseases but also to individuals without programming skills, offering a cost-free alternative to traditional commercial software. The solver can be run in parallel and represents, along with OpenFOAM, an open-source tool that can be employed for early detection and diagnosis of atherosclerosis and other cardiovascular diseases. Moreover, the algorithm is an open-source code, which makes it easy to implement enhancements or changes to adapt the solver to the user's requirements. A potential improvement to address in the future would be to include the interaction of wall deformation with hemodynamics to obtain more accurate WSS values, which are essential for assessing the risk of plaque rupture.

NOMENCLATURE

δ	average cell size
$\dot{\gamma}$	shear rate
Γ	domain boundary
$\mathbf{n}_b$	outward unit normal to the boundary
$\mathbf{u}$	velocity field
μ_f	fluid dynamic viscosity
ν_f	fluid kinematic viscosity
Ω	problem domain
$\overline{U}$	mean inlet velocity
ϕ	LDL concentration
ϕ_0	initial LDL concentration
ϕ_w	LDL concentration at the arterial wall
ρ_f	fluid density
τ	viscous stress tensor
τ_w	wall shear stress
A	artery inlet surface area
D	diameter or artery equivalent inlet diameter
d	number of space dimensions
g	gravity acceleration
Gr	Grashof number
K	LDL diffusivity
M_w	overall mass transfer coefficient
p	total pressure
p'	dynamic pressure
Pr	Prandtl number
q_{in}	mean blood inflow rate
r	radial coordinate measured from the centerline of the tube
r_m	local radius of the section
Re	Reynolds number
T	temperature

t	time
t_0	initial time
T_c	cardiac cycle
T_f	final time
U	axial velocity
V_w	water filtration velocity
X	axial distance measured from the throat of the constriction
$\mathbf{q}_\phi$	LDL flux

AUTHOR CONTRIBUTIONS

Jorge Molina: investigation (lead); methodology (lead); software (lead); validation (lead); writing – original draft (lead). **Daniel Rhys Obaid:** data curation (lead); resources (lead); writing – review and editing (equal). **A. S. Ademiloye:** data curation (equal); methodology (equal); supervision (lead); validation (equal); writing – original draft (equal); writing – review and editing (equal).

ACKNOWLEDGMENTS

CONFLICT OF INTEREST STATEMENT

The authors declare no potential conflict of interest.

DATA AVAILABILITY STATEMENT

The source code of the numerical model presented in this article, including ad-hoc boundary and initial conditions, is publicly available in the GitHub repository: https://github.com/JAMolina90/OpenFOAM_Artery.

ENDNOTES

*Note that in OpenFOAM's incompressible solvers, only the kinematic viscosity of the fluid has to be specified, then pressure and stress results are expressed in m²/s².

†The average cell size for three-dimensional meshes is defined as $\delta = \sqrt[3]{\frac{\sum_{i=1}^{n} V_i}{N}}$, where V_i represents the volume of cell i, and N is the total number of cells.

‡WSS can be computed in OpenFOAM by defining the corresponding function in the *controlDict* file.

ORCID

Jorge Molina https://orcid.org/0000-0001-7985-409X
Daniel Rhys Obaid https://orcid.org/0000-0002-3891-1403
A. S. Ademiloye https://orcid.org/0000-0002-9741-6488

REFERENCES

1. World Health Organization. Cardiovascular diseases (CVDs). 2021. https://www.who.int/news-room/fact-sheets/detail/cardiovascular -diseases-(cvds)
2. Man JJ, Beckman JA, Jaffe IZ. Sex as a biological variable in atherosclerosis. *Circ Res*. 2020;126:1297-1319.
3. Kannel WB. Overview of atherosclerosis. *Clin Ther*. 1998;20:B2-B17.
4. Sakellarios A, Bourantas CV, Papadopoulou SL, et al. Prediction of atherosclerotic disease progression using LDL transport modelling: a serial computed tomographic coronary angiographic study. *Eur Heart J Cardiovasc Imaging*. 2017;18:11-18.
5. De Nisco G, Zhang P, Calò K, et al. What is needed to make low-density lipoprotein transport in human aorta computational models suitable to explore links to atherosclerosis? Impact of initial and inflow boundary conditions. *J Biomech*. 2018;68:33-42.
6. Libby P. Inflammation in atherosclerosis. *Arterioscler Thromb Vasc Biol*. 2012;32:2045-2051.
7. Seely S. Atherosclerosis or hardening of the arteries? *Int J Cardiol*. 1989;22:5-12.
8. Arzani A. Coronary artery plaque growth: a two-way coupled shear stress–driven model. *Int J Numer Method Biomed Eng*. 2020;36:e3293.
9. Nielsen LB. Transfer of low density lipoprotein into the arterial wall and risk of atherosclerosis. *Atherosclerosis*. 1996;123:1-15.
10. Ross R, Glomset JA. The pathogenesis of atherosclerosis: (first of two parts). *N Engl J Med*. 1973;295:369-377.

11. Brown MS, Goldstein JL. How LDL receptors influence cholesterol and atherosclerosis. *Sci Am*. 1984;251:58-69.

12. Peiffer V, Sherwin SJ, Weinberg PD. Does low and oscillatory wall shear stress correlate spatially with early atherosclerosis? A systematic review. *Cardiovasc Res*. 2013;99:242-250.

13. Timmins LH, Molony DS, Eshtehardi P, et al. Oscillatory wall shear stress is a dominant flow characteristic affecting lesion progression patterns and plaque vulnerability in patients with coronary artery disease. *J R Soc Interface*. 2017;14:20160972.

14. Mekheimer KS, Shahzadi I, Nadeem S, Moawad AMA, Zaher AZ. Reactivity of bifurcation angle and electroosmosis flow for hemodynamic flow through aortic bifurcation and stenotic wall with heat transfer. *Phys Scr*. 2021;96:015216.

15. Alimohammadi M, Pichardo-Almarza C, Agu O, Díaz-Zuccarini V. Development of a patient-specific multi-scale model to understand atherosclerosis and calcification locations: comparison with in vivo data in an aortic dissection. *Front Physiol*. 2016;7:238.

16. Lantz J, Karlsson M. Large eddy simulation of LDL surface concentration in a subject specific human aorta. *J Biomech*. 2012;45:537-542.

17. Rostam-Alilou AA, Safari M, Jarrah HR, Zolfagharian A, Bodaghi M. A machine learning model for non-invasive detection of atherosclerotic coronary artery aneurysm. *Int J Comput Assist Radiol Surg*. 2022;17:2221-2229.

18. Morgan B, Murali AR, Preston G, et al. A physics-based machine learning technique rapidly reconstructs the wall-shear stress and pressure fields in coronary arteries. *Front Cardiovasc Med*. 2023;10:1221541.

19. Kafi O, El Khatib N, Tiago J, Sequeira A. Numerical simulations of a 3D fluid-structure interaction model for blood flow in an atherosclerotic artery. *Math Biosci Eng*. 2017;14:179.

20. Li X, Liu X, Zhang P, et al. Numerical simulation of haemodynamics and low-density lipoprotein transport in the rabbit aorta and their correlation with atherosclerotic plaque thickness. *J R Soc Interface*. 2017;14:20170140.

21. Pleouras DS, Sakellarios AI, Tsompou P, et al. Simulation of atherosclerotic plaque growth using computational biomechanics and patient-specific data. *Sci Rep*. 2020;10:1-14.

22. Doradla P, Otsuka K, Nadkarni A, et al. Biomechanical stress profiling of coronary atherosclerosis: identifying a multifactorial metric to evaluate plaque rupture risk. *JACC Cardiovasc Imaging*. 2020;13:804-816.

23. Piemjaiswang R, Ding Y, Feng Y, et al. Effect of transport parameters on atherosclerotic lesion growth: a parameter sensitivity analysis. *Comput Methods Programs Biomed*. 2021;199:105904.

24. Pignani A, Di Venuta I, Boghi A, Gori F. Mass transfer and blood flow in a patient-specific three-dimensional Willis circle. *Int Commun Heat Mass Transf*. 2021;126:105369.

25. Ahadi F, Biglari M, Azadi M, Bodaghi M. Computational fluid dynamics of coronary arteries with implanted stents: effects of Newtonian and non-Newtonian blood flows. *Eng Rep*. 2023;6:e12779.

26. Weller HG, Tabor G, Jasak H, Fureby C. A tensorial approach to computational continuum mechanics using object-oriented techniques. *Comput Phys*. 1998;12:620-631.

27. Ahrens J, Geveci B, Law C. ParaView: an end-user tool for large data visualization. *Visualization Handbook*. Elsevier; 2005.

28. Arthurs CJ, Khlebnikov R, Melville A, et al. CRIMSON: an open-source software framework for cardiovascular integrated modelling and simulation. *PLoS Comput Biol*. 2021;17:e1008881.

29. Updegrove A, Wilson NM, Merkow J, et al. SimVascular: an open source pipeline for cardiovascular simulation. *Ann Biomed Eng*. 2017;45:525-541.

30. Molina J, Ortiz P. A continuous finite element solution of fluid interface propagation for emergence of cavities and geysering. *Comput Methods Appl Mech Eng*. 2020;359:112746.

31. Schrauwen JT, Coenen A, Kurata A, et al. Functional and anatomical measures for outflow boundary conditions in atherosclerotic coronary bifurcations. *J Biomech*. 2016;49:2127-2134.

32. Soulis JV, Fytanidis DK, Papaioannou VC, Styliadis H, Giannoglou GD. Oscillating LDL accumulation in normal human aortic arch-shear dependent endothelium. *Hippokratia*. 2011;15:22.

33. Asgharzadeh H, Borazjani I. Effects of Reynolds and Womersley numbers on the hemodynamics of intracranial aneurysms. *Comput Math Methods Med*. 2016;2016:7412926.

34. Wada S, Karino T. Theoretical prediction of low-density lipoproteins concentration at the luminal surface of an artery with a multiple bend. *Ann Biomed Eng*. 2002;30:778-791.

35. Zhang LW, Ademiloye AS, Liew KM. A multiscale Cauchy–Born meshfree model for deformability of red blood cells parasitized by plasmodium falciparum. *J Mech Phys Solids*. 2017;101:268-284.

36. Ademiloye AS, Zhang LW, Liew KM. A multiscale framework for large deformation modeling of RBC membranes. *Comput Methods Appl Mech Eng*. 2018;329:144-167.

37. Casson N. A flow equation for pigment-oil suspensions of the printing ink type. *Rheology of Disperse Systems*. Pergamon Press; 1959:84-104.

38. Venkatesan J, Sankar DS, Hemalatha K, Yatim Y. Mathematical analysis of Casson fluid model for blood rheology in stenosed narrow arteries. *J Appl Math*. 2013;2013:583809.

39. Jamil DF, Saleem S, Roslan R, et al. Analysis of non-Newtonian magnetic Casson blood flow in an inclined stenosed artery using Caputo-Fabrizio fractional derivatives. *Comput Methods Programs Biomed*. 2021;203:106044.

40. Fournier RL. *Basic Transport Phenomena in Biomedical Engineering*. CRC Press; 2017.

41. Issa RI. Solution of the implicitly discretised fluid flow equations by operator-splitting. *J Comput Phys*. 1986;62:40-65.

42. Iwatsu R, Hyun JM, Kuwahara K. Mixed convection in a driven cavity with a stable vertical temperature gradient. *Int J Heat Mass Transf*. 1993;36:1601-1608.

43. Ahmed SA, Giddens DP. Velocity measurements in steady flow through axisymmetric stenosed at moderate Reynolds numbers. *J Biomech*. 1983;16:505-516.

44. Varghese SS, Frankel SH, Fischer PF. Direct numerical simulation of stenotic flows. Part 1. Steady flow. *J Fluid Mech*. 2007;582:253-280.

45. Chr1sC0de: ArteryScalingLawsBC (Github repository). 2020. Accessed October 15, 2022. https://github.com/Chr1sC0de/ArteryScalingLawsBC

46. Peng C, Liu J, He W, et al. Numerical simulation in the abdominal aorta and the visceral arteries with or without stenosis based on 2D PCMRI. *Int J Numer Method Biomed Eng*. 2021;38:e3569.

47. Torii R, Wood NB, Hadjiloizou N, et al. Fluid-structure interaction analysis of a patient-specific right coronary artery with physiological velocity and pressure waveforms. *Commun Numer Methods Eng*. 2009;25:565-580.

48. Sakellarios A, Tsompou P, Kigka V, et al. Non-invasive prediction of site-specific coronary atherosclerotic plaque progression using lipidomics, blood flow, and LDL transport modeling. *Appl Sci*. 2021;11:1976.

49. Oviedo C, Maehara A, Mintz GS, et al. Intravascular ultrasound classification of plaque distribution in left main coronary artery bifurcations: where is the plaque really located? *Circ Cardiovasc Interv*. 2010;3:105-112.

50. Morbiducci U, Kok AM, Kwak BR, Stone PH, Steinman DA, Wentzel JJ. Atherosclerosis at arterial bifurcations: evidence for the role of haemodynamics and geometry. *Thromb Haemost*. 2016;115:484-492.

51. Zhou M, Yu Y, Chen R, et al. Wall shear stress and its role in atherosclerosis. *Front Cardiovasc Med*. 2023;10:1-11.

52. Kikinis R, Pieper SD, Vosburgh K. 3D slicer: a platform for subject-specific image analysis, visualization, and clinical support. In: Jolesz FA, ed. *Intraoperative Imaging Image-Guided Therapy*. Springer; 2014.

53. Tian Y, Li X, Zhao B, Zhang J, Liang F. Influence of morphological characteristics on the deposition of low-density lipoprotein in intracranial bifurcation aneurysms. *Phys Fluids*. 2023;35:081905.

54. Nooraeen A, Ghalichi F, Taghizadeh H, Guidoin R. Probing the possibility of lesion formation/progression in vicinity of a primary atherosclerotic plaque: a fluid–solid interaction study and angiographic evidences. *Int J Numer Method Biomed Eng*. 2022;38:e3605.

APPENDIX A. VELOCITY WAVEFORMS

The time-dependent velocity law imposed at the inflow boundary is given by Equation (8), whose coefficients a_k and b_k have been computed for two arterial velocity profiles shown in References 32 (fig. 2) and 33 (fig. 3). These waveforms are represented in Figure A1, and amplitudes are detailed in Table A1.
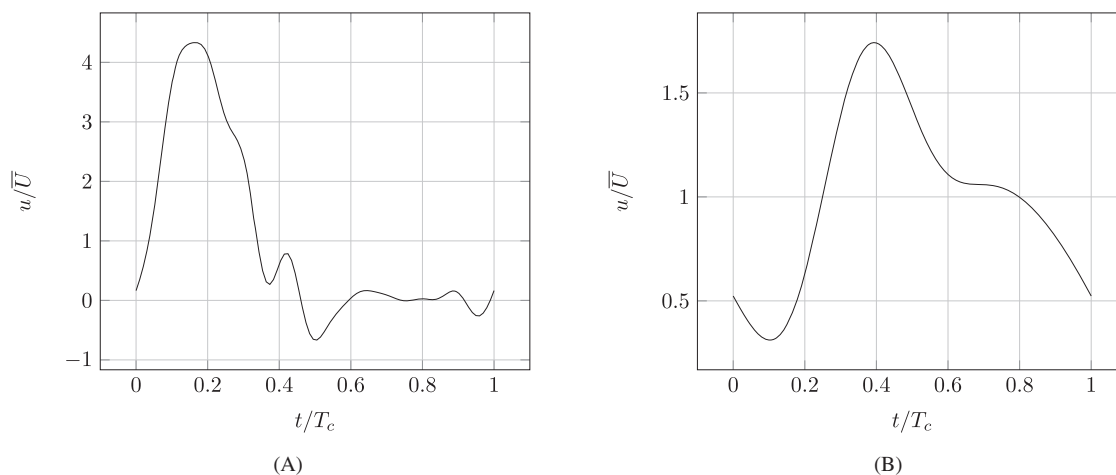

FIGURE A1 Velocity waveforms profiles. (A) Waveform 1.[32] (B) Waveform 2.[33]

T A B L E A1 Amplitudes a_k and b_k for two human heartbeat velocity profiles.

k	Waveform 1[32]		Waveform 2[33]	
	a_k	b_k	a_k	b_k
1	0.71819	1.61140	−0.51083	0.00933
2	−0.81339	0.81890	−0.02449	−0.29734
3	−0.41610	0.04217	0.05868	0.02950
4	−0.27150	−0.11101	-	-
5	−0.06379	0.07506	-	-
6	−0.13346	−0.11824	-	-
7	0.12152	0.01844	-	-
8	−0.08979	0.04770	-	-
9	0.05685	−0.08896	-	-
10	0.05572	0.03879	-	-